SCIENCE CHINA
Life Sciences

•RESEARCH PAPER•

October 2022 Vol.65 No.10: 1971–1984
https://doi.org/10.1007/s11427-021-2099-7

Identification of serum metabolites enhancing inflammatory responses in COVID-19

Chen-Song Zhang[1†], Bingchang Zhang[2†], Mengqi Li[1†], Xiaoyan Wei[1†], Kai Gong[2†], Zhiyong Li[3], Xiangyang Yao[4], Jianfeng Wu[1], Cixiong Zhang[1], Mingxia Zhu[1], Lei Zhang[1], Xiufeng Sun[1], Yi-Hong Zhan[2], Zhengye Jiang[5], Wenpeng Zhao[5], Wei Zhong[5], Xinguo Zhuang[3,5], Dawang Zhou[1], Hai-Long Piao[6], Sheng-Cai Lin[1*] & Zhanxiang Wang[2,7*]

[1]*State Key Laboratory for Cellular Stress Biology, School of Life Sciences, Xiamen University, Xiamen 361102, China;*
[2]*Department of Neurosurgery, Xiamen Key Laboratory of Brain Center, the First Affiliated Hospital of Xiamen University, Xiamen 361102, China;*
[3]*Department of Laboratory Medicine, The First Affiliated Hospital of Xiamen University, Xiamen 361102, China;*
[4]*Department of pulmonary diseases, The First Affiliated Hospital of Xiamen University, Xiamen 361102, China;*
[5]*School of Medicine, Xiamen University, Xiamen 361102, China;*
[6]*Scientific Research Center for Translational Medicine, Dalian Institute of Chemical Physics, Chinese Academy of Sciences, Dalian 116023, China;*
[7]*Institute of Neurosurgery, School of Medicine, Xiamen University, Xiamen 361102, China*

Received December 21, 2021; accepted March 22, 2022; published online April 28, 2022

Coronavirus disease 2019 (COVID-19), caused by severe acute respiratory syndrome coronavirus 2 (SARS-CoV-2), is characterized by a strong production of inflammatory cytokines such as TNF and IL-6, which underlie the severity of the disease. However, the molecular mechanisms responsible for such a strong immune response remains unclear. Here, utilizing targeted tandem mass spectrometry to analyze serum metabolome and lipidome in COVID-19 patients at different temporal stages, we identified that 611 metabolites (of 1,039) were significantly altered in COVID-19 patients. Among them, two metabolites, agmatine and putrescine, were prominently elevated in the serum of patients; and 2-quinolinecarboxylate was changed in a biphasic manner, elevated during early COVID-19 infection but levelled off. When tested in mouse embryonic fibroblasts (MEFs) and macrophages, these 3 metabolites were found to activate the NF-κB pathway that plays a pivotal role in governing cytokine production. Importantly, these metabolites were each able to cause strong increase of TNF and IL-6 levels when administered to wildtype mice, but not in the mice lacking NF-κB. Intriguingly, these metabolites have little effects on the activation of interferon regulatory factors (IRFs) for the production of type I interferons (IFNs) for antiviral defenses. These data suggest that circulating metabolites resulting from COVID-19 infection may act as effectors to elicit the peculiar systemic inflammatory responses, exhibiting severely strong proinflammatory cytokine production with limited induction of the interferons. Our study may provide a rationale for development of drugs to alleviate inflammation in COVID-19 patients.

COVID-19, metabolites, inflammation

Citation: Zhang, C.S., Zhang, B., Li, M., Wei, X., Gong, K., Li, Z., Yao, X., Wu, J., Zhang, C., Zhu, M., et al. (2022). Identification of serum metabolites enhancing inflammatory responses in COVID-19. Sci China Life Sci 65, 1971–1984. https://doi.org/10.1007/s11427-021-2099-7

†Contributed equally to this work
*Corresponding authors (Sheng-Cai Lin, email: linsc@xmu.edu.cn; Zhanxiang Wang, email: wangzx@xmu.edu.cn)

INTRODUCTION

The pandemic of coronavirus disease 2019 (COVID-19), caused by the severe acute respiratory syndrome coronavirus 2 (SARS-CoV-2), has cost the life of over 4 million people worldwide in less than two years. COVID-19 patients show broad clinical manifestations, from asymptomatic to rapid fatalities (Chen et al., 2020; Huang et al., 2020a; Wang et al., 2020a). Clinical descriptions on immunological features of COVID-19 patients have revealed distinct clinical features characterized by an excessive production of circulating proinflammatory cytokines such as IL-1β, IL-6, IL-17, TNF, type II IFN (IFNγ) by innate immune cells, which is known as ‘‘cytokine storm’’, and is closely associated with patient mortality (Del Valle et al., 2020; Karki et al., 2021; Laing et al., 2020; Liu et al., 2020; Long et al., 2020; Mulchandani et al., 2021; Schultze and Aschenbrenner, 2021; Sette and Crotty, 2021; Wang et al., 2020b). Therapies for neutralizing IL-6 and TNF directly with monoclonal antibodies have shown promising efficacy in treating COVID-19 patients (Rosas et al., 2021; Salama et al., 2021; Waggershauser et al., 2020), underscoring the importance of these cytokines in causing excessive immune responses. However, how these cytokines are abnormally produced during SARS-CoV-2 infection remains unclear. As with other coronaviruses, SARS-CoV-2 is recognized by the endosomal sensors Toll-like receptors, or the cytosolic sensors retinoic acid-inducible gene 1 (RIG-I) and melanoma differentiation-associated gene 5 (MDA5) (Li et al., 2010; Mazaleuskaya et al., 2012; Zheng et al., 2021). These signalosomes activate tumor necrosis factor receptor-associated factor (TRAF) 3 and TRAF6, which in turn phosphorylate and activate the inhibitory κB (IκB) kinase complex (IKK complex). IKK then phosphorylates and activates NF-κB complex by phosphorylating Ser932 of the p105 subunit of the NF-κB complex, leading to the cleavage of p105 into p50. IKK also phosphorylates the Ser536 of p65 subunit. The phosphorylated p65 and p50 then form a complex and act as a master transcription factor, mediating the expression of a series of genes including those encoding the cytokines involved in the cytokine storm (Zhang et al., 2017). In parallel, the activated TRAF3 and TRAF6 are also supposed to stimulate the interferon regulatory factor (IRF) pathways for the antiviral responses via phosphorylating and activating the TANK binding kinase 1 (TBK1), which in turn phosphorylates IRF3 and 7 to induce the transcription of type I IFNs, such as IFNα and IFNβ, and interferon-stimulated genes (ISGs) for antiviral defenses (Sa Ribero et al., 2020). However, despite the shared molecular mechanisms for NF-κB and IRFs, the IRF pathway is poorly activated in COVID-19 patients: an enhanced expression of proinflammatory cytokines with low ISGs. This leads to exuberant inflammatory responses with little innate antiviral defenses (Blanco-Melo et al., 2020; Hadjadj et al., 2020; Xiong et al., 2020). Longitudinal analysis further revealed an unusual temporal distribution of ISGs and proinflammatory cytokines induction during COVID-19: ISGs, likely of lung origin, are induced only during early infection—level off afterwards (Banerjee et al., 2020; Gordon et al., 2020; Konno et al., 2020; Lei et al., 2020; Xia et al., 2020)—which is followed by persistently high levels of proinflammatory cytokines, particularly in severe patients (Arunachalam et al., 2020; Liu et al., 2021; Lucas et al., 2020).

RESULTS

We started by determining the serum levels of various metabolites in a cohort of 78 subjects, including 30 healthy controls and 48 COVID-19 patients. All patients were hospitalized in the First Affiliated Hospital of Xiamen University and were supplied with similar hospital meals hence minimizing the interference from diets in metabolites. Patients were categorized to mild and severe groups, according to their oxygenation index ($PaO_2/FiO_2 \leq 300$ mmHg as the severe, see detailed clinical indices in Table S1 and Figure S1 in Supporting Information), and serum samples were collected weekly for 5 weeks, and at 2 or 4 week after discharge from hospital as a control (diagramed in Figure S2A and B in Supporting Information). Considering the highly variable chemical properties of metabolites in the serum, different mass spectrometry (MS)-based approaches, including HPLC-MS, GC-MS and CE-MS (all targeted), were applied to analyze small polar metabolites (metabolome) and lipids (lipidome) of the COVID-19 patients. As summarized in Table S2 in Supporting Information, a total of 1,039 metabolites (with 597 polar metabolites, and 442 lipids) were analyzed; 611 metabolites (312 polar metabolites, and 299 lipids) were significantly changed (either increased, decreased, or fluctuated) during the course of COVID-19 infection (see also Figure 1A and B, among which the metabolites with $P<0.001$ are shown as heatmaps, and Figure S3A and B in Supporting Information for graphs of all metabolites). Kyoto Encyclopedia of Genes and Genomes (KEGG) pathway enrichment analyses of polar metabolites showed that various amino acid metabolic pathways, such as arginine biosynthesis pathways, were listed as the top dysregulated pathways during the course of COVID-19 (Figure 2A), as previously reported (Shen et al., 2020; Thomas et al., 2020). Significant differences of polar metabolites between patients and healthy controls were further supported by the principal component analysis (PCA), through which the data of patients and healthy controls could be separated into two distinct clusters/datasets (Figure 2B). By contrast, the lipidomic metabolites between COVID-19 patients and healthy controls showed no difference between the two groups by

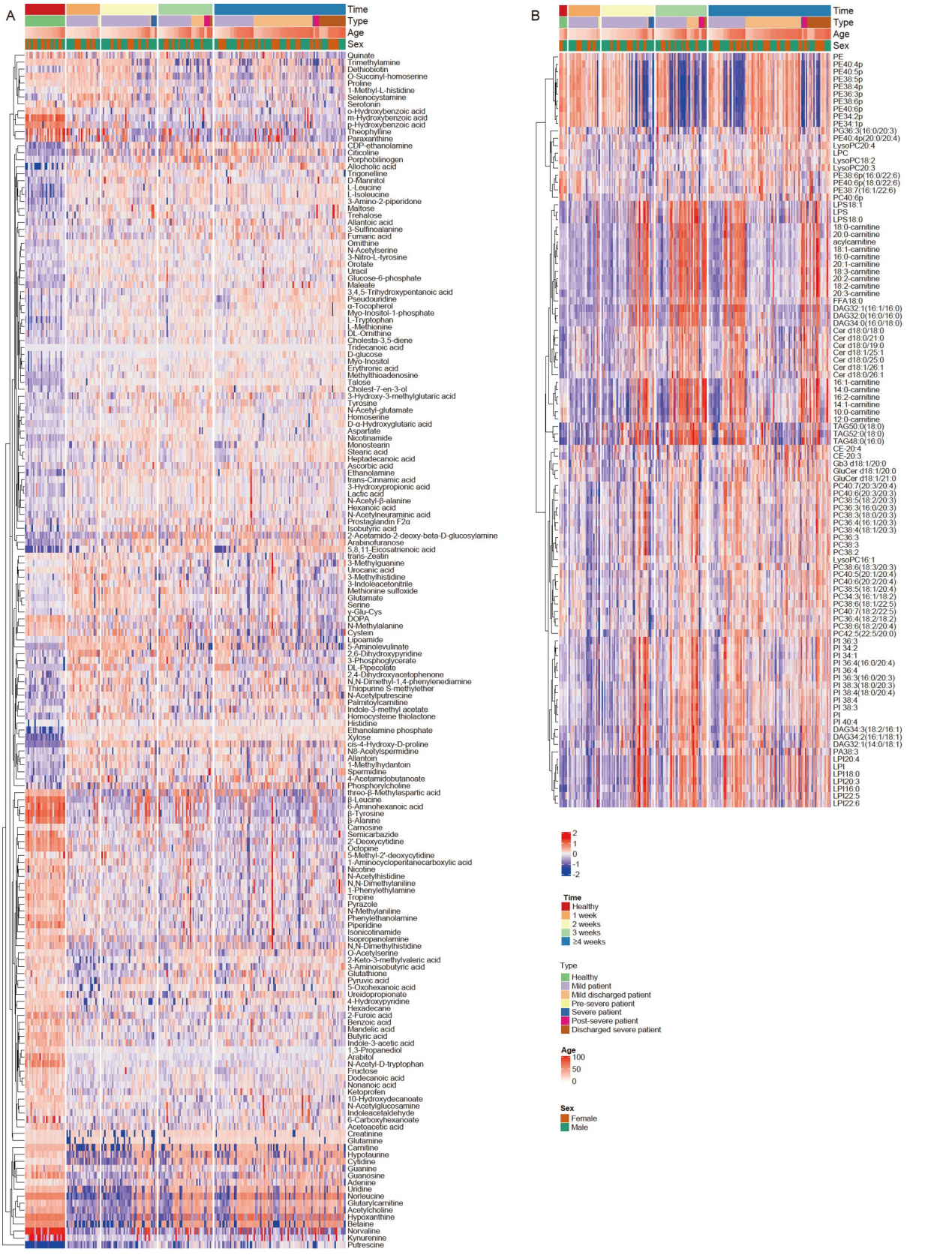

Figure 1 Overview of metabolomic features in patients with COVID-19. A and B, Heatmap showing the levels of polar metabolites (A) and lipids (B) that are significantly changed (P<0.001) in the serum of COVID-19 patients. Rows were clustered/split by hierarchical clustering on metabolites. Columns were split by the time from symptom onset, and were additionally annotated with sample types (mild, discharged mild, pre-severe, severe, post-severe, or discharged severe patients, or healthy controls), age and sex. See also Figures S1–S3 in Supporting Information.

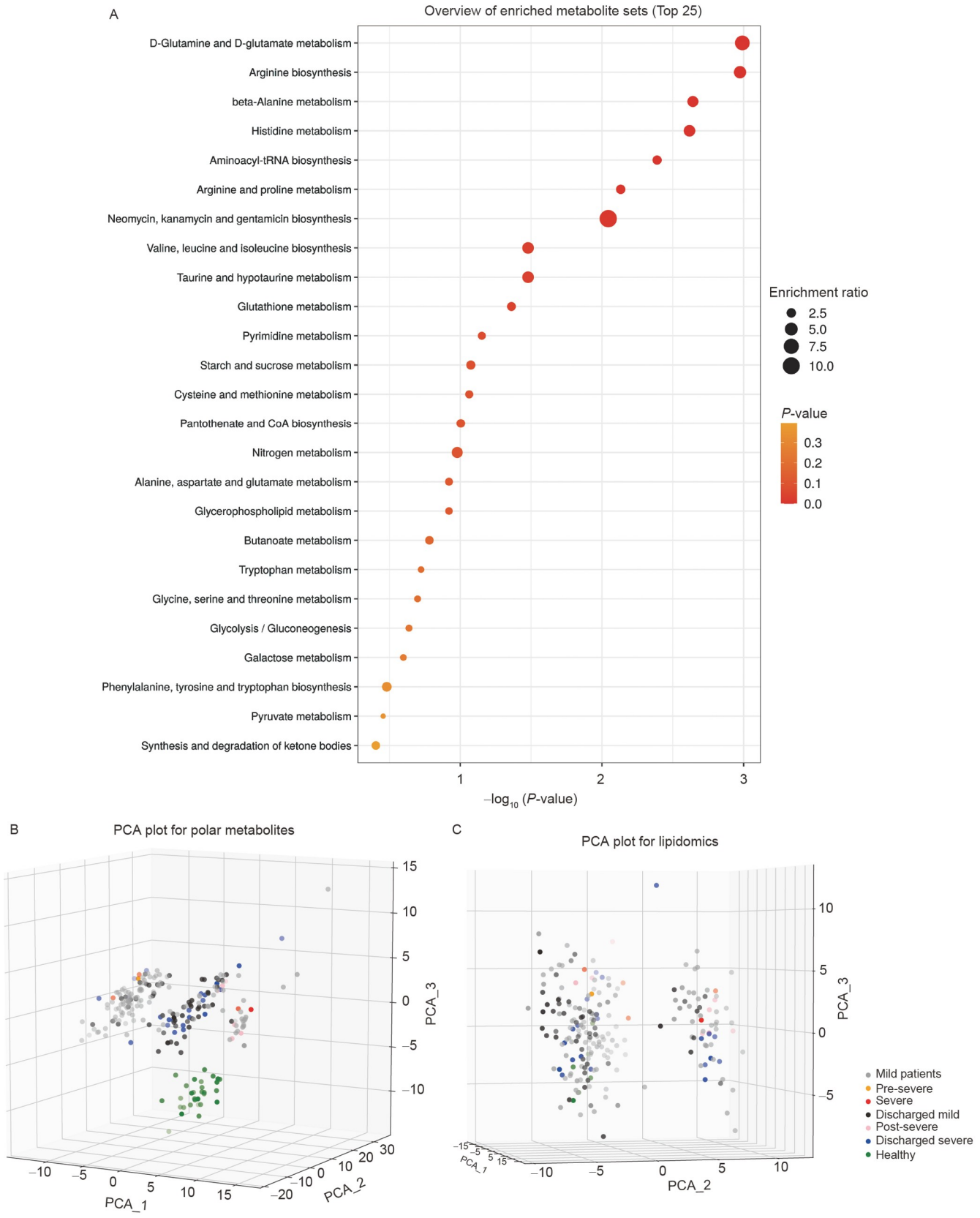

Figure 2 Significantly changed polar metabolites in COVID-19 patients. A, Top 25 KEGG pathways based on pathway enrichment analyses of polar metabolites measured in the serum of COVID-19 patients. B and C, PCA of polar metabolites (B) and lipids (C). The PCA map is annotated with sample types, categorized as mild patients (grey solid circle), discharged mild (black solid circle), pre-severe (orange solid circle), severe (red solid circle), post-severe (pink solid circle), discharged severe (blue solid circle), and healthy control (green solid circle).

PCA (Figure 2C). We hereafter focused on the altered 312 polar metabolites that showed significant changes (133 increased, 107 decreased, and 72 fluctuated, as summarized in Table S3 in Supporting Information) between the controls and the COVID-19 patients.

We next tested whether these 133 metabolites that are increased during the COVID-19 infection contribute to the inflammatory responses by determining whether they could activate the NF-κB pathway, a pivotal indicator for the immune responses, in mouse embryonic fibroblasts (MEFs). Those metabolites were individually added into the cell culture medium, i.e., DMEM. As for the concentrations of the metabolites used in the screening assays, we referred to published studies (see Table S3 in Supporting Information). For metabolites that have not yet been tested, we set 1 mmol L^{-1} as the highest concentration, given that most abundant metabolites lie in such a range; the concentrations were gradually decreased if adversary effects such as cytotoxicity occurred (Table S3 in Supporting Information). Through such a screening process, we identified that agmatine and putrescine, almost undetectable in healthy controls but significantly increased in patients, could activate the NF-κB pathway, as determined by the increased levels of p-Ser536 on p65, p-Ser932 on p105 of the NF-κB complex, and p-Ser172 on TBK1 (Figure 3A and B; Table S3 in Supporting Information). Neither agmatine nor putrescine could inhibit the NF-κB pathway as determined using TNFα-pretreated MEFs, excluding the possibility that these two metabolites could also act as a feedback system to tune down the overly activated NF-κB pathway in COVID-19 patients (Figure 3C and D). Therefore, the increased agmatine and putrescine are direct activators of the NF-κB pathway. We also tested the possibility that the metabolites that are decreased (107 in total) during the infection may exert a role to inhibit the immune response, under the rationale that lack of the inhibitory effects by those metabolites leads to over production of the proinflammatory cytokines. These metabolites were individually added to the TNFα-pretreated MEFs, and found that none of the metabolites showed an inhibitory effect (Table S3 in Supporting Information). For the metabolites that are fluctuated during COVID-19 (72 in total), both the activation and the inhibition on NF-κB signaling were examined, by using regularly cultured MEF cells and TNFα-pretreated MEFs respectively. In this category, we found that 2-quinolinecarboxylate (2-QC), which was found to be increased at week 1, and then decreased between weeks 2 to 3 and remained low thereafter, could activate the NF-κB pathway (Figure 3E; Table S3 in Supporting Information), and could not inhibit the NF-κB pathway when added to the TNFα-pretreated MEFs (Figure 3F). We showed that the 3 metabolites identified were all capable of activating the NF-κB pathway in mouse primary macrophages (Figure 3G). Intriguingly, we found that none of these metabolites can promote the phosphorylation of IRFs, i.e., p-Ser396 of IRF3, which are responsible for the production of the type I interferons (Figure 3H), although they could promote the phosphorylation of their upstream kinase, TBK1 (Figure 3A, B and E) in MEFs, in which the IRF signaling is intact (Figure 3H).

We next determined whether these 3 metabolites could activate the NF-κB pathway in the mouse as seen in COVID-19 patients. To better reflect the pathogenic situation, we titrated the dosage of these 3 metabolites to reach the concentrations seen in COVID-19 patients. Of note, absolute concentrations of agmatine and putrescine —calculated by standard curves generated via the corresponding isotopes, were shown. In comparison, relative concentrations of 2-quinolinecarboxylate were shown, because of lacking the commercially available isotope. We found that mice intraperitoneally injected with agmatine at 3 mg kg^{-1}, putrescine at 120 mg kg^{-1}, and 2-quinolinecarboxylate at 200 mg kg^{-1} could lead to an accumulation of each metabolite to the peak concentration detected in the serum of patients (Figure S4A–C in Supporting Information). Such a dosage of each metabolite could activate the NF-κB pathway in various mouse peripheral tissues, including skeletal muscle, liver, lung, kidney and heart (Figure 4A–C). We also tested their effects on inflammatory cytokine secretion in mice, and found that agmatine significantly elevated TNF and IL-6, all downstream effectors of NF-κB (Figure 4D). Similarly, putrescine significantly elevated TNF, IL-6 and IL-10 (Figure 4E), and 2-quinolinecarboxylate significantly elevated TNF and IL-6 (Figure 4F). We then determined if the effects of these three metabolites on cytokine secretion were dependent on the NF-κB pathway, and found that in mice lacking p105/p50 of NF-κB and hence NF-κB signaling (Kanters et al., 2004; Sha et al., 1995), none of these metabolites could affect cytokine secretion (Figure 4G). Of note, all these three metabolites failed to elevate the levels of IL-1β (Figure S4D in Supporting Information), indicating that other factors may be accounted for stimulating such a proinflammatory cytokine in COVID-19 patients. We also found that none of these three metabolites could induce the production of IFNα and IFNβ, two type I IFNs (Figure 4H), consistent with the inability of the metabolites to induce IRF phosphorylation and activation (Figure 3H).

DISCUSSION

Our results therefore have identified specific metabolites that are changed in abundance during the COVID-19 infection, and contribute to the production and secretion of inflammatory cytokines. We have directly pinned down the stimulating effect of these metabolites on the transcriptional activity of the NF-κB pathway in MEFs and macrophages, and have recapitulated these effects at the organismal level

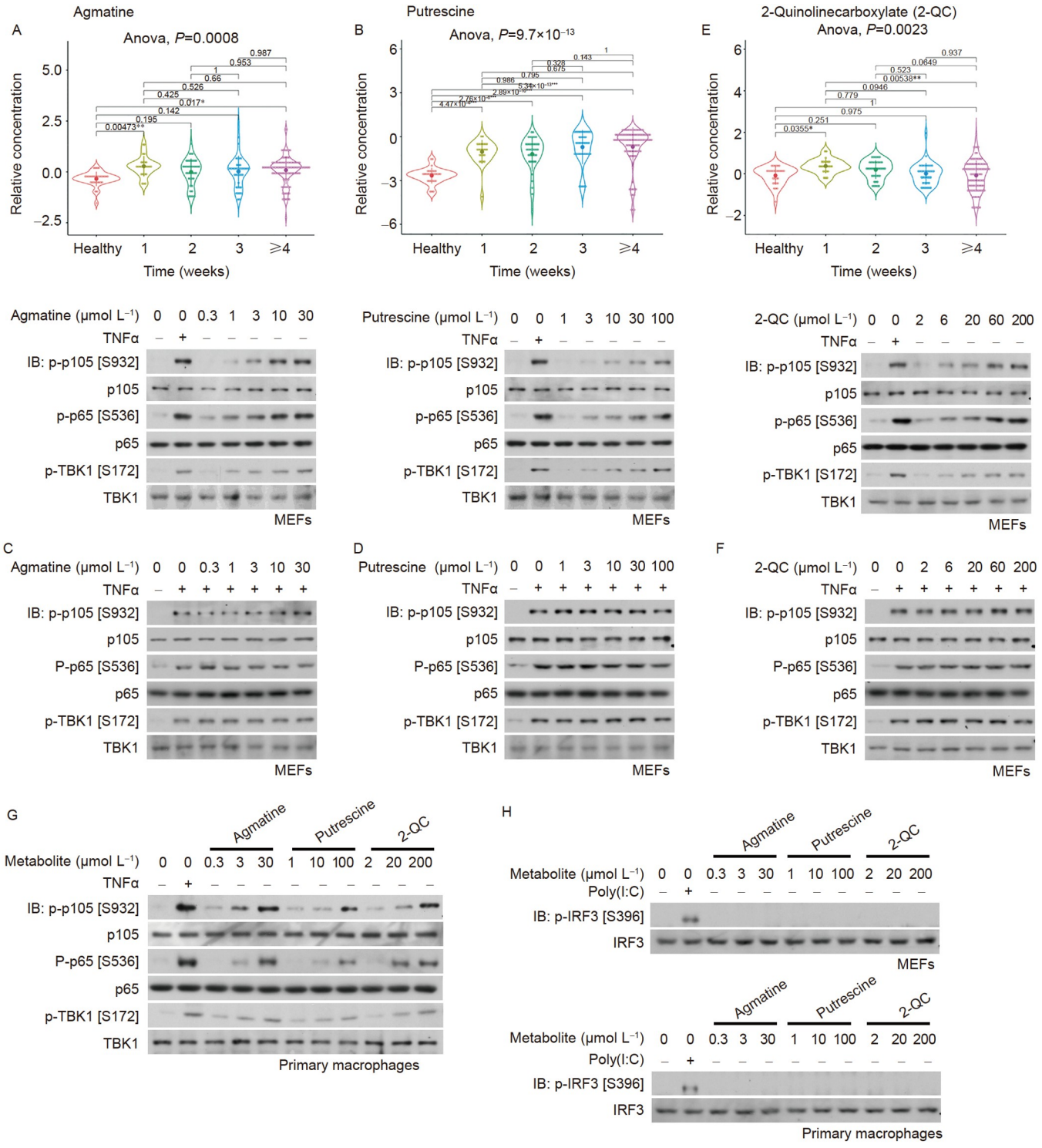

Figure 3 Agmatine, putrescine, and 2-QC can activate the NF-κB, but not the IRF pathway. A–G, Agmatine, putrescine and 2-QC activate the NF-κB pathway. Metabolites at indicated concentrations were added to MEFs (A–F) or primary macrophages (G) for 1 h. Some 15-min treatment of TNFα at 10 μmol L^{-1} was applied before cell harvesting. Levels of p-Ser932 on p105, and p-Ser536 on p65 of the NF-κB, and the p-Ser172 on the TBK1 were then determined by immunoblotting. See also relative levels of agmatine (A), putrescine (B) and 2-QC (E) during COVID-19 on the upper side of each panel. H, Agmatine, putrescine and 2-QC fail to lead to IRF phosphorylation. Agmatine, putrescine and 2-QC at indicated concentrations were added to MEFs (upper) or primary macrophages (lower) for 2 h. As a control, cells were transfected with poly(I:C) for 2 h. Levels of p-IRF3 (Ser396) were determined by immunoblotting.

by using the mouse model. Importantly, all of the three metabolites identified here are increased during the first week after the onset of COVID-19 symptom, closely matching the time point when proinflammatory cytokines are

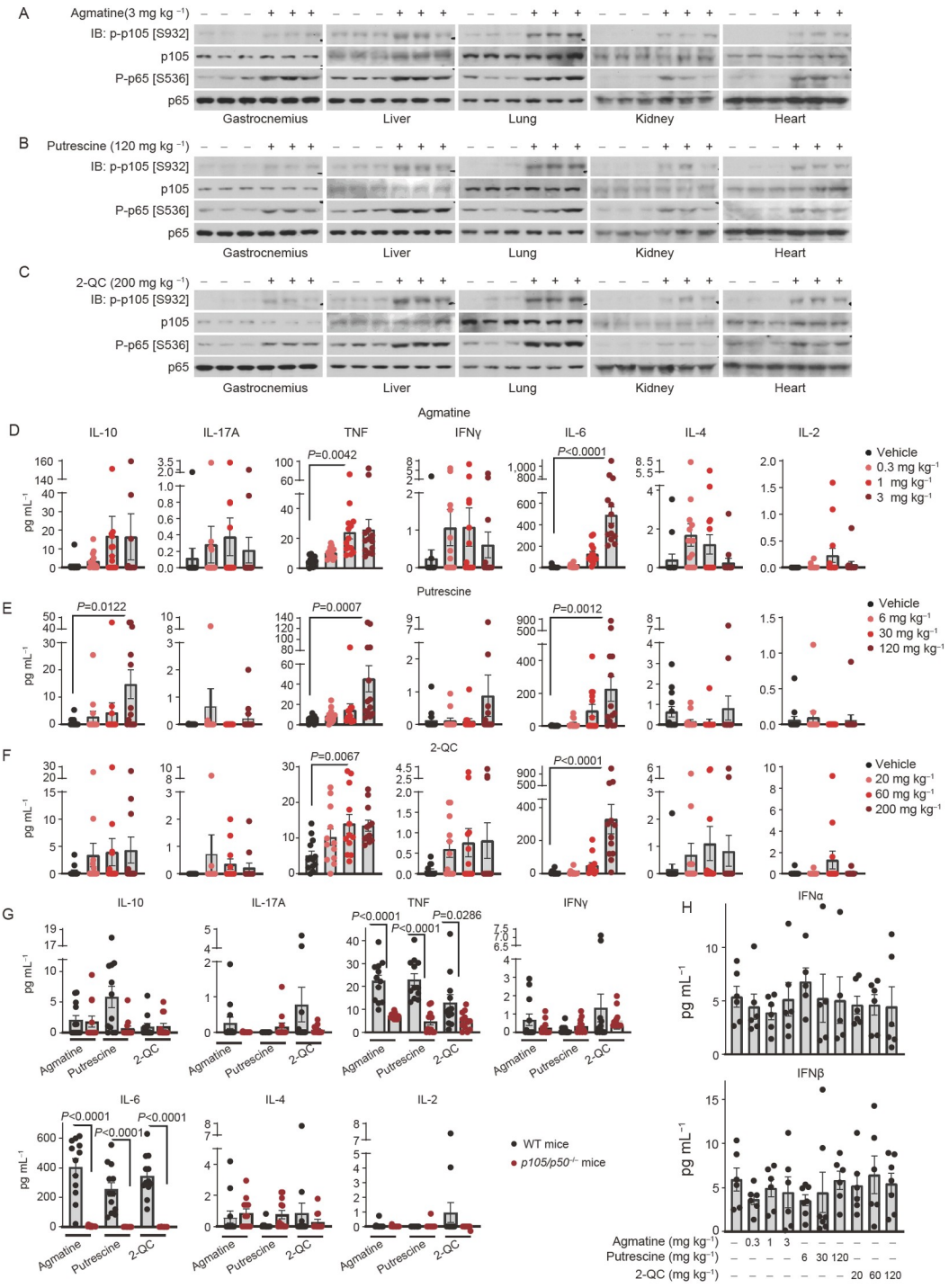

Figure 4 Recapitulation of the stimulation of proinflammatory response but not antiviral response by agmatine, putrescine, and 2-QC in mice. A–C, Agmatine, putrescine and 2-QC activate the NF-κB pathway in mouse tissues. Agmatine at 3 mg kg^{-1} (A), putrescine at 120 mg kg^{-1} (B), or 2-QC at 200 mg kg^{-1} (C) were each intraperitoneally injected to mice. At 1 h (A),2 h (B) or 10 h (C) after injection, levels of p-p105 and p-p65 of NF-κB in gastrocnemius muscle, liver, lung, kidney and heart were determined by immunoblotting. D–F, Agmatine, putrescine, and 2-QC promote the production of inflammatory cytokines. Mice were administered with agmatine, putrescine or 2-QC at indicated concentrations, followed by collecting serum at 1 h (D), 2 h (E) or 10 h (F). Levels of IL-2, IL-4, IL-6, IL-10, IL-17A, IFNγ and TNF were then analyzed and are graphed as mean±SEM; n=12−14 for each metabolite/concentration; P value by one-way ANOVA, followed by Dunnett. See also levels of IL-1β in Figure S4D in Supporting Information. G, Knockout of NF-κB blocks the effects of agmatine, putrescine and 2-QC on inflammatory cytokine production. Mice with knockout of *p105*/*p50* of NF-κB, along with their wildtype littermates, were administered with each of the three metabolites as in (A) to (C). Inflammatory cytokines were then analyzed and are graphed as mean±SEM; n=12 for each metabolite/concentration; P value by two-way ANOVA, followed by Sidak. H, Agmatine, putrescine, and 2-QC fail to promote the production of type I IFNs. Mice were treated with three metabolites as in (D–F). Levels of IFNα (upper) and IFNβ (lower) were then analyzed and are graphed as mean±SEM; n=5–6 for each metabolite/concentration; P value by one-way ANOVA, followed by Tukey. See also Figure S4 in Supporting Information.

induced (Blanco-Melo et al., 2020; Lucas et al., 2020). We also found that none of these metabolites could promote the production of type I IFNs, which are often induced to combat viral infection. The observed excessive proinflammatory responses coupled with a lack of boosting antiviral defenses in the presence of these metabolites mirror the imbalanced immune response seen in COVID-19: when systemic inflammatory responses are triggered within 1 week after the symptom onset, the ISG system does not seem to respond and remains at a minimal level (Arunachalam et al., 2020; Liu et al., 2021; Lucas et al., 2020). At this stage, we do not have the exact mechanism through which such a preferential activation of the NF-κB pathway by these three metabolites was achieved, given that none of the three metabolites identified in this study have been reported to be physically or functionally linked to such a signaling. One possible explanation is that the three metabolites can bind to and be sensed by their receptors such as GPCRs, as do TLRs to trigger the NF-κB pathway. For example, it has been shown that spermidine is a ligand/agonist of calcium-sensing receptor (CaSR), a class C GPCR, and stimulates the ability of CaSR in calcium releasing (Quinn et al., 1997; Rogers et al., 2015). Although the role(s) of CaSR in regulating NF-κB has not been examined, both GPCR (such as S1PR) and calcium have long been recognized as modulators of NF-κB (Berry et al., 2018; Siehler et al., 2001). Apart from the three metabolites identified in this study, many endogenous metabolites such as succinate (Mills et al., 2016), α-ketoglutarate (Cheng et al., 2019) and lactate (Samuvel et al., 2009), have been shown to be able to regulate the NF-κB pathway. Although not all of the receptor(s) of them have been identified, it has been shown that GPR81 is the receptor of lactate for triggering the NF-κB pathway (Samuvel et al., 2009), reinforcing the potential roles of GPCR in sensing metabolites to control inflammatory responses. As for the failure of the three metabolites in activating the IRF pathway, it might be explained by the fact that exogenous (i.e., viral) DNA and RNA, but not endogenous metabolites, are stimuli for IRF. In this study, we found that none of the three metabolites could elicit the phosphorylation of IRF3, which is different from poly(I:C), a synthetic analogue of double-stranded RNA (Figure 3H). Among the three metabolites, agmatine and putrescine belong to a branch of polyamine biosynthesis pathway in which arginine is converted to agmatine by arginine decarboxylase (ADC), then to putrescine by agmatinase. Putrescine is further catabolized to other polyamines such as spermidine and spermine. Consistent with our observation, it has been shown that during the COVID-19, the levels of arginine are decreased, while the levels of putrescine and its derivative, N-acetylputrescine and spermidine, are significantly elevated (Gassen et al., 2021; Shen et al., 2020; Thomas et al., 2020; Wu et al., 2021), suggesting an increased rate of polyamine biosynthesis from arginine. It was also reported that the seral levels of spermidine and acetylspermidine are positively correlated with the levels of the proinflammatory IL-6 (Thomas et al., 2020). Together with the findings that inhibition of polyamine biosynthesis can impair the replication of many kinds of coronaviruses (Huang et al., 2020b), the polyamine biosynthesis pathway may also be a potential therapeutic target, not only a biomarker, for COVID-19.

LIMITATIONS OF STUDY

Our study has a limitation: due to the limited number of local patients, there were only 9 severe COVID-19 patients hospitalized at the designated, First Affiliated Hospital of Xiamen University, among which 6 had become mild before enrollment for blood collection (Figure S2 in Supporting Information), and 5 were suffering from underlying medical comorbidities such as diabetes which may affect the serum metabolites. Therefore, metabolomic data obtained from severe cases in this study may not be sufficiently informative for profiling the serum metabolome of severe COVID-19 patients, which is consistent with the PCA data showing that severe cases cannot be separated from mild cases (Figure 2B and C). Nevertheless, data from our validation experiments using the NF-κB system tested in both MEFs and mouse models, which plays a causal role in the elevation of immune cytokines, support a positive correlation between the polyamine content and the disease severity (Thomas et al., 2020).

Our study, owing to the limitation mentioned above, in fact revealed the metabolic changes, and the specific metabolites responsible for triggering NF-κB signaling, in mild patients. Based on the ability of the three metabolites to activate the NF-κB signaling, we pondered a possibility of the metabolites causing severe symptoms in severe patients, who might have higher magnitude of enhancement of NF-κB signaling. Of note, no difference in lipidomic data can be observed between mild patients and healthy persons, while other studies have shown alterations in serum lipid contents of severe patients, and have proposed that changes in lipid contents contribute to the hyperinflammatory phase of severe COVID-19 (Huang et al., 2020c; Lam et al., 2021; Song et al., 2020). Therefore, it is possible that the metabolites discovered in our study might act together with those changed lipids species to cause hyperinflammatory responses in severe patients. However, further studies are needed for a formal suggestion.

MATERIALS AND METHODS

Patients

COVID-19 patients (between 16 and 75 years old) admitted

to the First Affiliated Hospital of Xiamen University (the solely designated hospital for the treatment of COVID-19 in Xiamen, China) between January 22 2020 and April 24 2020 were enrolled in this study. Patients were diagnosed by SARS-CoV-2 RT-PCR testing on a respiratory sample (nasopharyngeal swab) according to WHO interim guidance. No statistical methods were used to predetermine sample size. There were 48 patients, along with 30 healthy controls (22 to 67 years old) with a negative SARS-CoV-2 RT-PCR testing at the time of enrollment, were included in this study, and both groups were subjected to consecutive monitoring by the RT-PCR test. The study design was approved by the Ethics Committee of First Affiliated Hospital of Xiamen University (No. 2020-001), and was in accordance with the Helsinki Declaration and Good Clinical Practice. All participants signed an informed consent form before enrollment.

Mice

The *p105*/*p50*$^{-/-}$ mice (Jackson Laboratory, #006097, USA) were obtained from Jackson Laboratory, provided by Dr. Menno de Winther. Protocols for all mouse experiments were approved by the Institutional Animal Care and the Animal Committee of Xiamen University (XMU-LAC20180028). Mice were housed with free access to water and standard diet (65% carbohydrate, 11% fat, 24% protein). The light was on from 8 a.m. to 8 p.m. Male littermate controls were used throughout the study. Genotypes were confirmed by PCR analysis with primers Forward: 5′-ATA GGC AAG GTC AGA ATG CAC CAG AAG TCC-3′ and Reverse1: 5′-GCA AAC CTG GGA ATA CTT CAT GTG ACT AAG-3′, and Reverse2: 5′-AAA TGT GTC AGT TTC ATA GCC TGA AGA ACG-3′ for *p105*/*p50*$^{-/-}$ mice.

Patient demographics

Demographic information, as summarized on Table S1 in Supporting Information, was aggregated through a standard data collecting form, and was extracted from the electronic medical record (EMRs). Considering the broad clinical manifestations and hence variance in interpretation of the time from infection, the times of symptom onset of COVID-19 patients were determined using following guidelines: (i) highest priority of criteria for estimating the onset was given to explicit onset dates provided by patients; (ii) second highest priority was given to the earliest reported symptom by a patient; and (iii) in the absence of direct information regarding symptom onset, we estimated a date through manual assessment of the EMRs by an independent clinician. Mild and severe groups were determined according to their oxygenation index, as $PaO_2/FiO_2 \leq 300$ mmHg are severe COVID-19 patients. The clinical team, separate from the investigators, diagnosed, treated patients, and performed chart reviews to determine relevant statistics. Blood collection was also performed by the clinical team, and investigators were unaware of the patients' conditions during sample processing and subsequent mass spectrometry studies. Information on patients' conditions was not available until finishing the analysis of metabolomic data.

Laboratory blood examinations

The laboratory blood examinations included: (i) routine blood tests (C-reactive protein levels, neutrophil counts, monocyte counts, basophils counts, eosinophils counts, lymphocyte counts, white blood cell counts, red blood cell counts, and platelet counts), performed on an automated hematology analyzer (BC-5390 CRP, Mindray, Shenzhen, China); (ii) coagulation tests (D-dimer, prothrombin time, international normalized ratio, thrombin time, activated partial thromboplastin time, fibrinogen, and fibrin degradation products), performed on an automated coagulation analyzer (CS-2000i, Sysmex, Shanghai, China); (iii) biochemical tests (γ-glutamyl transpeptidase, lactate dehydrogenase, carbon dioxide, low density lipoprotein, urea, uric acid, total cholesterol, total bilirubin, total protein, chlorinum, osmolality, triglyceride, albumin, direct bilirubin, alkaline phosphatase, phosphorus, creatinine, creatine kinase, creatine kinase isoenzyme MB, blood glucose, alanine aminotransferase, aspartate aminotransferase, apolipoprotein A1, apolipoprotein B, blood calcium, blood sodium, blood potassium, blood magnesium, indirect bilirubin, high density lipoprotein), performed on a clinical chemistry analyzer (DxC 800, Beckman, USA); and (iv) calcitonin levels, analyzed on a compact immunoanalyzer (VIDAS, Biomerieux, France).

Serum metabolome determination

For measuring serum metabolome, blood samples were collected between February 18 2020 and April 24 2020 in the morning before breakfast, aliquoted from those collected in routine care, and were process on the same day of collection. The blood samples (approximately 10 mL) were collected in Vacutainer™ SST™ II Advance Tubes (BD, USA), and were placed at room temperature for 10 min, followed by centrifugation at 3,000×*g* at 4°C for another 10 min. The upper layer was serum.

To analyze polar metabolites via HPLC-MS and CE-MS, some 400 μL of serum was instantly mixed with 2 mL of precooled methanol (Sigma-Aldrich, USA) containing IS1 (1:200 dilution, Human Metabolome Technologies, Japan), then mixed with 2 mL of chloroform (Sigma-Aldrich) and 800 μL of water (containing 4 μg mL^{-1} [U-^{13}C]-glutamine (Cambridge Isotope Laboratories, USA), followed with 20 s of vortexing. After centrifugation at 15,000×*g* for another

15 min at 4°C, the supernatant (aqueous phase) was then divided into 3 portions: (a) 600 μL, for HPLC-MS analysis; (b) 400 μL, for CE-MS analysis on anion mode; and (c) 400 μL, for CE-MS analysis on cation mode. Portion (a) was then freeze-dried in a vacuum concentrator (Labconco, CentriVap Benchtop Centrifugal Vacuum Concentrator, equipped with a CentriVap −84°C Cold Trap and a Scroll Vacuum Pump) at 4°C, and then dissolved in 100 μL of 50% (v/v, in water) acetonitrile (Sigma-Aldrich), followed by centrifugation at 15,000×*g* for another 30 min at 4°C. Some 2 μL of supernatant were loaded onto a HILIC column (ZIC-pHILIC, 5 μm, 2.1 mm×100 mm, PN: 1.50462.0001, Millipore, USA) on a UPLC system (ExionLC AD, SCIEX, USA) which is interfaced with a QTRAP MS (SCIEX, QTRAP 5500). The mobile phase consisted of 15 mmol L^{-1} ammonium acetate (Sigma-Aldrich) containing 3 mL L^{-1} ammonium hydroxide (>28%, v/v; Sigma-Aldrich) in the LC-MS grade water (mobile phase A), and LC-MS grade 90% (v/v) acetonitrile in LC-MS grade water (mobile phase B), and was run at a flow rate of 0.2 mL min^{-1}. The HPLC gradient elution program was: 95% B held for 2 min, then to 45% B in 13 min, held for 3 min, and then back to 95% B for 4 min. Each sample was analyzed on both the positive and the negative modes on the HPLC-MS. The mass spectrometer was run on a Turbo V ion source with spray voltages of −4,500 V (negative mode) and 5,500 V (positive mode), source temperature at 550°C, Gas No.1 at 50 psi, Gas No.2 at 55 psi, and curtain gas at 40 psi. Metabolites were measured using the multiple reactions monitoring mode (MRM), and declustering potentials and collision energies were optimized through using analytical standards. The relative amounts of metabolites were analyzed by MultiQuant Software (AB SCIEX). Portions (b) and (c) of supernatant were then filtrated through a 5-kDa cutoff filter (Millipore, UFC3LCCNB-HMT, USA) by centrifuging at 12,000×*g* for 3 h at 4°C. The filtered aqueous phase was then freeze-dried at 4°C, and then dissolved in 100 μL of water containing IS3 (1:200 for portion (b), or 1:400 for portion (c); Human Metabolome Technologies). Some 20 μL of redissolved potion (b) and portion (c) solutions were then loaded into injection vials (with conical inserts) for CE-QTOF MS (Agilent Technologies 7100, equipped with 6545 mass spectrometer) analysis on cation and anion modes, respectively. For cation mode, the mobile phase consisted of 1 mol L^{-1} formic acid, and the voltage applied on the capillary was 27 kV. For anion mode, 50 mmol L^{-1} ammonium acetate (pH 8.5) and 30 kV were used. The mass spectrometer was run on a Dual AJS ESI ion source. For cation mode, parameters for mass spectrometer were set as follows: Gas Temp at 300°C, Drying Gas at 7 L min^{-1}, Nebulizer at 5 psi, Sheath Gas Temp at 100°C, Sheath Gas Flow at 8 L min^{-1}, VCap at 3,500 V, Nozzle Voltage at 2,000 V, Fragmentor at 80 V, Skimmer at 50 V, and Oct 1RF Vpp at 500 V. Parameters for anion mode were set as those of cation mode, except that VCap at 3,000 V, and Fragmentor at 110 V. Data were processed using Qualitative Analysis (B.06.00) from Agilent (USA).

For determination of the absolute concentrations of agmatine and putrescine, samples were prepared as those for HPLC-MS measurements. Some 1 μL (for agmatine) or 5 μL (for putrescine) of re-dissolved supernatants were loaded onto a HILIC column (Atlantis Silica HILIC, 3 μm, 2.1 mm×150 mm, Waters, USA) on a UPLC system (SCIEX, ExionLC AD) interfaced with a QTRAP MS (SCIEX, QTRAP 6500 plus). The mobile phase consisted of 10 mmol L^{-1} ammonium acetate containing 0.1% formic acid (v/v) in the LC-MS grade water (mobile phase A), and 0.1% formic acid (v/v) in LC-MS grade acetonitrile (mobile phase B), and was run at a flow rate of 0.35 mL min^{-1}. The HPLC gradient elution program was: 80% B, then to 30% B in 5 min, held for 2 min, and then back to 80% B for 3 min. The mass spectrometer was run on a Turbo V ion source and running in positive mode. Compounds were measured using the MRM, and declustering potentials and collision energies were optimized through using analytical standards. The following transitions were used for monitoring each compound: 89/30 for putrescine, 131/72 for agmatine, and 152/88 for [U-^{13}C]-glutamine. Standard curve generated from isotope-labelled agmatine or putrescine were run alongside samples await being quantified. Data were analyzed by MultiQuant Software (AB SCIEX).

To analyze polar metabolites via GC-MS, some 400 μL of serum was instantly mixed with 1.6 mL of methanol containing 40 μg mL^{-1} tridecanoic acid as an internal standard, followed with 20 s of vortexing. After centrifugation at 15,000×*g* for 15 min at 4°C, 400 μL of supernatant (aqueous phase) was freeze-dried at 4°C. The lyophilized sample was then vortexed for 1 min after mixing with 50 μL of freshly prepared methoxyamine hydrochloride (20 mg mL^{-1} in pyridine (Sigma-Aldrich)), followed by incubating at 4°C for 1 h. The mixture was sonicated at 0°C by bathing in ice slurry for 10 min, and was then incubated at 37°C for 1.5 h, followed by mixing with 50 μL of MSTFA (Sigma-Aldrich) and incubated at 37°C for 1 h. Before subjecting to GC-MS, sample was centrifuged at 15,000×*g* for 10 min, and some 60 μL of supernatant was loaded into an injection vial. GC was performed on a HP-5MS column (30 m×0.25 mm i.d., 0.25 μm film thickness) using a GC/MSD instrument (7890-5977B, Agilent). The injector temperature was 260°C. The column oven temperature was first held at 70°C for 2 min, then increased to 180°C at the rate of 7°C min^{-1}, then to 250°C at the rate of 5°C min^{-1}, then to 310°C at the rate of 25°C min^{-1}, where it was held for 15 min. The MSD transfer temperature was 280°C. The MS quadrupole and source temperature were maintained at 150°C and 230°C, respectively. Data were analyzed using MassHunter software (B.07.01SP1) from Agilent.

Lipidomics was performed by LipidALL Technologies Co., Ltd. (Changzhou, China), following the protocols as described previously (Song et al., 2020). Briefly, lipids were extracted according to a modified version of the Bligh and Dyer's protocol (Lu et al., 2019). For each sample, 100 μL of serum was used. The organic phase of each sample was freeze-dried, and was resuspended in 100 μL of chloroform: methanol 1:1 (v/v) spiked with appropriate concentrations of internal standards (Song et al., 2020). All lipidomic analyses were carried out on an Exion UPLC coupled with a SCIEX QTRAP 6500 PLUS system as described previously, using an extensive, targeted library tailored for human serum lipidome that confers sufficient lipid coverage to render global lipid pathway analysis (Lu et al., 2019). All quantification experiments were conducted using internal standard calibration as described previously (Shui et al., 2010).

Cell culture and peritoneal macrophage isolation

Cells, including MEFs and peritoneal macrophages, were maintained in DMEM (Gibco, USA) supplemented with 10% FBS (Gibco), 100 IU penicillin, 100 mg mL^{-1} streptomycin at 37°C in a humidified incubator containing 5% CO_2. For determining the effects of a metabolite among the formulation list of DMEM (such as amino acids) on the NF-κB pathway, a customized DMEM medium without such a kind of metabolite was used.

Peritoneal macrophages were elicited by thioglycollate before isolation as described previously (Rodriguez et al., 2019). Briefly, C57BL/6 mice were intraperitoneally injected with 1 mL of sterilized, 3% thioglycollate (BD). On the day 3, mice were euthanized by cervical dislocation, and the peritoneal cells were collected via peritoneal lavage by 5 mL (per mouse) of PBS. The lavage fluid was centrifuged for 5 min at 1,000×*g* and was resuspended in 5 mL of Red blood cell lysis buffer (Sigma-Aldrich), followed by rotating for another 5 min. The suspension was centrifuged for 5 min at 3,000×*g*, and then resuspended in DMEM supplemented with 10% inactivated (55°C for 30 min) FBS. Cells were then seeded in 12-well plates at a density of 1.2×10^6 cells per well. Culture medium was refreshed after 6 h of cell seeding. Poly(I:C) (R&D Systems, USA) was transfected using Lipofectamine™ RNAiMAX (Thermo Fisher Scientific, USA). Some 0.1 μg of Poly(I:C), mixed with 6 μL of Lipofectamine™ RNAiMAX was added to cells grown to 80% confluence in a well of a 12-well dish.

Immunoblotting

To analyze the levels of phosphorylated p65 (Ser536), p105 (Ser932), TBK1 (Ser172) and IRF3 (Ser396) in MEFs, cells at 70%–80% confluence in a well of a 6-well dish were lysed with 300 μL of ice cold lysis buffer (20 mmol L^{-1} Tris-HCl (Sigma-Aldrich), pH 7.5, 150 mmol L^{-1} NaCl (Sigma-Aldrich), 1 mmol L^{-1} EDTA (Sigma-Aldrich), 1 mmol L^{-1} EGTA (Sigma-Aldrich), 1% Triton X-100 (Sigma-Aldrich), 2.5 mmol L^{-1} sodium pyrophosphate, 1 mmol L^{-1} β-glycerolphosphate (Sigma-Aldrich), with protease and phosphatase inhibitor cocktail). The lysates were then sonicated and centrifuged at 20,000×*g* for 10 min at 4°C, and the supernatant was mixed with a quarter volume of 5× SDS (Sigma-Aldrich) sample buffer. Levels of phosphorylated p65, p105, TBK1 and IRF3 in macrophages were similarly determined, except that cells at 80% confluence from a well of a 12-well plate were lyzed with 100 μL of 1.2× SDS sample buffer. Samples were boiled for 10 min before running SDS-PAGE. Levels of total proteins and phosphorylated proteins were analyzed on separate gels, and representative immunoblots were shown. The antibodies used for Western blotting were as follows: p65 (1:1,000 dilution, CST, USA), phosphorylated p65 (Ser536) (1:1,000 dilution, CST), p105 (1:1,000 dilution, CST), phosphorylated p105 (Ser932) (1:1,000 dilution, CST), TBK1 (1:1,000 dilution, CST), phosphorylated TBK1 (Ser172) (1:1,000 dilution, CST), IRF3 (1:1,000 dilution, CST), phosphorylated IRF3 (Ser396) (1:1,000 dilution, CST), HRP-conjugated goat anti-rabbit IgG antibody (1:5,000 dilution, Jackson ImmunoResearch, USA).

Cytokine determination

Levels of serum IL-2, IL-4, IL-6, IL-10, IL-17A, IFNγ and TNF were determined by a mouse Th1/Th2/Th17 CBA kit (BD) on a flow cytometer (LSRFortessa X-20) according to the manufacturer's instruction. Briefly, some 50 μL of freshly prepared serum, 50 μL of mixed capture beads suspension, and 50 μL of PE detection reagents were gently mixed, followed by incubation for 2 h at room temperature in the dark. Samples were then washed and resuspended, then analyzed flow cytometer. Data were analyzed using FCAP Array software (v3) from BD. Levels of serum IL-1β were measured by an IL-1β ELISA kit (Thermo Fisher Scientific) according to the manufacturer's instruction, in which 100 μL of serum was used in each measurement. Note that the 96-well plate (Nunc™ MaxiSorp™) used should be coated by the capture antibody overnight at 4°C prior to the experiment. Levels of IFNα/β were measured by Mouse Interferon alpha ELISA Kit (Abcam, UK) and Mouse IFN beta ELISA Kit (Abcam) according to the manufacture's instruction, in which 50 μL of 3-fold diluted serum for IFNα, and 2-fold diluted serum for IFNβ (diluted by Sample Diluent NS) were used in each assay.

Metabolomic data processing

Data for lipids and polar metabolites were separately analyzed. All negative values and zero values were replaced by a

fifth of the least positive value of each metabolite. Data were then $\log_{10}$ transformed, and were normalized by Pareto scaling, through which each value was mean-centered and was then divided by the square root of the standard deviation.

Data for each metabolite were grouped based on the sampling time (week 1, week 2, week 3, and ≥week 4 after the symptom onset), along with healthy controls as the normal group. Multiple comparisons among these 5 groups were performed using a one-way ANOVA followed by Tukey's multiple comparisons by the rstatix package (0.7.0) for R software (4.0.1). The metabolites with significant differences (with overall ANOVA $P<0.05$) were chosen for screening the effects on NF-κB pathway, and those $P<0.001$ for generating the heatmaps by the ComplexHeatmap package (2.4.3) for R software. "Increased", "decreased" and "fluctuated" metabolites were determined based on the mean value of each group, and the P value between groups (obtained from Tukey's multiple comparisons). Note that metabolites with all P values from multiple comparisons above 0.05 were considered as "fluctuated".

PCA was performed by the Scikit-learn package for Python (0.22.1). Three principal components were extracted through the PCA, and the three-dimensional scatter plots were drawn for lipids and polar metabolites, respectively, allowing to see the distribution of difference among various subjects. KEGG pathway analysis was conducted through the MetaboAnalyst5.0 online tool (at https://www.metaboanalyst.ca/), in which the polar metabolites with overall ANOVA $P<0.001$ were included.

Statistical analysis

Statistical analysis for data shown on Figures 1 and 2, Figures S1–S4 and Table S2 in Supporting Information was performed by R software (4.0.1). Scatter plots and line charts were generated by Python (3.7.4) software with Matplotlib (3.1.1) and Seaborn (0.9.0) libraries. The Kruskal-Wallis test was used to compare ages of patients among different groups, and Pearson's Chi-squared test with Yates' continuity correction for categorical factors. All P values were two-sided. For other figures and tables, statistical analyses were performed using Prism 9 (GraphPad Software). Each group of data was subjected to Kolmogorov-Smirnov test, Anderson-Darling test, D'Agostino-Pearson omnibus test or Shapiro-Wilk test for normal distribution when applicable. For comparisons between multiple groups, an ordinary one-way ANOVA was used, followed by Tukey, Sidak, or Dunnett as specified in the legends. The assumptions of homogeneity of error variances were tested using F-test ($P>0.05$). For comparison between multiple groups with two fixed factors, an ordinary two-way ANOVA was used, followed by Sidak's multiple comparisons test as specified in the legends. Geisser-Greenhouse's correction was used where applicable. For all data, differences were considered significant when $P<0.05$.

Compliance and ethics *The author(s) declare that they have no conflict of interest.*

Acknowledgements *This work was supported by the National Natural Science Foundation of China (31922034, 82088102, 91854208, 92057204, 31730058, 82072777), Science and Technology Program of Fujian Provincial Health Commission (2021ZD02006), Xiamen Science and Technology Major Project (3502Z2020YJ05), Xiamen Municipal Bureau of Science and Technology (3502Z20209005), Fundamental Research Funds for the Central Universities (20720200014, 20720200069, 20720190084), and Program of Introducing Talents of Discipline to Universities (BP2018017). We acknowledge all health care workers involved in the diagnosis and treatment of patients in the First Affiliated Hospital of Xiamen University, and all the patients, supporters, and their families for their confidence in our work. We also thank Dr. Menno de Winther (Academic Medical Center, Universiteit Utrecht) for providing p105/p50$^{-/-}$ mice (Jackson Laboratory, #006097).*

References

Arunachalam, P.S., Wimmers, F., Mok, C.K.P., Perera, R.A.P.M., Scott, M., Hagan, T., Sigal, N., Feng, Y., Bristow, L., Tak-Yin Tsang, O., et al. (2020). Systems biological assessment of immunity to mild versus severe COVID-19 infection in humans. Science 369, 1210–1220.

Banerjee, A.K., Blanco, M.R., Bruce, E.A., Honson, D.D., Chen, L.M., Chow, A., Bhat, P., Ollikainen, N., Quinodoz, S.A., Loney, C., et al. (2020). SARS-CoV-2 disrupts splicing, translation, and protein trafficking to suppress host defenses. Cell 183, 1325–1339.e21.

Berry, C.T., May, M.J., and Freedman, B.D. (2018). STIM- and Orai-mediated calcium entry controls NF-κB activity and function in lymphocytes. Cell Calcium 74, 131–143.

Blanco-Melo, D., Nilsson-Payant, B.E., Liu, W.C., Uhl, S., Hoagland, D., Møller, R., Jordan, T.X., Oishi, K., Panis, M., Sachs, D., et al. (2020). Imbalanced host response to SARS-CoV-2 drives development of COVID-19. Cell 181, 1036–1045.e9.

Chen, N., Zhou, M., Dong, X., Qu, J., Gong, F., Han, Y., Qiu, Y., Wang, J., Liu, Y., Wei, Y., et al. (2020). Epidemiological and clinical characteristics of 99 cases of 2019 novel coronavirus pneumonia in Wuhan, China: a descriptive study. Lancet 395, 507–513.

Cheng, M.X., Cao, D., Chen, Y., Li, J.Z., Tu, B., and Gong, J.P. (2019). α-ketoglutarate attenuates ischemia-reperfusion injury of liver graft in rats. Biomed pharmacother 111, 1141–1146.

Del Valle, D.M., Kim-Schulze, S., Huang, H.H., Beckmann, N.D., Nirenberg, S., Wang, B., Lavin, Y., Swartz, T.H., Madduri, D., Stock, A., et al. (2020). An inflammatory cytokine signature predicts COVID-19 severity and survival. Nat Med 26, 1636–1643.

Gassen, N.C., Papies, J., Bajaj, T., Emanuel, J., Dethloff, F., Chua, R.L., Trimpert, J., Heinemann, N., Niemeyer, C., Weege, F., et al. (2021). SARS-CoV-2-mediated dysregulation of metabolism and autophagy uncovers host-targeting antivirals. Nat Commun 12, 3818.

Gordon, D.E., Jang, G.M., Bouhaddou, M., Xu, J., Obernier, K., White, K. M., O'Meara, M.J., Rezelj, V.V., Guo, J.Z., Swaney, D.L., et al. (2020). A SARS-CoV-2 protein interaction map reveals targets for drug repurposing. Nature 583, 459–468.

Hadjadj, J., Yatim, N., Barnabei, L., Corneau, A., Boussier, J., Smith, N., Péré, H., Charbit, B., Bondet, V., Chenevier-Gobeaux, C., et al. (2020). Impaired type I interferon activity and inflammatory responses in severe COVID-19 patients. Science 369, 718–724.

Huang, C., Wang, Y., Li, X., Ren, L., Zhao, J., Hu, Y., Zhang, L., Fan, G., Xu, J., Gu, X., et al. (2020a). Clinical features of patients infected with 2019 novel coronavirus in Wuhan, China. Lancet 395, 497–506.

Huang, M., Zhang, W., Chen, H., and Zeng, J. (2020b). Targeting

polyamine metabolism for control of human viral diseases. Infect Drug Resist Volume 13, 4335–4346.
Huang, W., Li, C., Wang, Z., Wang, H., Zhou, N., Jiang, J., Ni, L., Zhang, X.A., and Wang, D.W. (2020c). Decreased serum albumin level indicates poor prognosis of COVID-19 patients: hepatic injury analysis from 2,623 hospitalized cases. Sci China Life Sci 63, 1678–1687.
Kanters, E., Gijbels, M.J.J., van der Made, I., Vergouwe, M.N., Heeringa, P., Kraal, G., Hofker, M.H., and de Winther, M.P.J. (2004). Hematopoietic NF-κB1 deficiency results in small atherosclerotic lesions with an inflammatory phenotype. Blood 103, 934–940.
Karki, R., Sharma, B.R., Tuladhar, S., Williams, E.P., Zalduondo, L., Samir, P., Zheng, M., Sundaram, B., Banoth, B., Malireddi, R.K.S., et al. (2021). Synergism of TNF-α and IFN-γ triggers inflammatory cell death, tissue damage, and mortality in SARS-CoV-2 infection and cytokine shock syndromes. Cell 184, 149–168.e17.
Konno, Y., Kimura, I., Uriu, K., Fukushi, M., Irie, T., Koyanagi, Y., Sauter, D., Gifford, R.J., Nakagawa, S., and Sato, K. (2020). SARS-CoV-2 ORF3b is a potent interferon antagonist whose activity is increased by a naturally occurring elongation variant. Cell Rep 32, 108185.
Laing, A.G., Lorenc, A., Del Molino Del Barrio, I., Das, A., Fish, M., Monin, L., Muñoz-Ruiz, M., McKenzie, D.R., Hayday, T.S., Francos-Quijorna, I., et al. (2020). A dynamic COVID-19 immune signature includes associations with poor prognosis. Nat Med 26, 1623–1635.
Lam, S.M., Zhang, C., Wang, Z., Ni, Z., Zhang, S., Yang, S., Huang, X., Mo, L., Li, J., Lee, B., et al. (2021). A multi-omics investigation of the composition and function of extracellular vesicles along the temporal trajectory of COVID-19. Nat Metab 3, 909–922.
Lei, X., Dong, X., Ma, R., Wang, W., Xiao, X., Tian, Z., Wang, C., Wang, Y., Li, L., Ren, L., et al. (2020). Activation and evasion of type I interferon responses by SARS-CoV-2. Nat Commun 11, 3810.
Li, J., Liu, Y., and Zhang, X. (2010). Murine coronavirus induces type I interferon in oligodendrocytes through recognition by RIG-I and MDA5. J Virol 84, 6472–6482.
Liu, C., Martins, A.J., Lau, W.W., Rachmaninoff, N., Chen, J., Imberti, L., Mostaghimi, D., Fink, D.L., Burbelo, P.D., Dobbs, K., et al. (2021). Time-resolved systems immunology reveals a late juncture linked to fatal COVID-19. Cell 184, 1836–1857.e22.
Liu, Y., Yang, Y., Zhang, C., Huang, F., Wang, F., Yuan, J., Wang, Z., Li, J., Li, J., Feng, C., et al. (2020). Clinical and biochemical indexes from 2019-nCoV infected patients linked to viral loads and lung injury. Sci China Life Sci 63, 364–374.
Long, Q.X., Tang, X.J., Shi, Q.L., Li, Q., Deng, H.J., Yuan, J., Hu, J.L., Xu, W., Zhang, Y., Lv, F.J., et al. (2020). Clinical and immunological assessment of asymptomatic SARS-CoV-2 infections. Nat Med 26, 1200–1204.
Lu, J., Lam, S.M., Wan, Q., Shi, L., Huo, Y., Chen, L., Tang, X., Li, B., Wu, X., Peng, K., et al. (2019). High-coverage targeted lipidomics reveals novel serum lipid predictors and lipid pathway dysregulation antecedent to type 2 diabetes onset in normoglycemic Chinese adults. Diabetes Care 42, 2117–2126.
Lucas, C., Wong, P., Klein, J., Castro, T.B.R., Silva, J., Sundaram, M., Ellingson, M.K., Mao, T., Oh, J.E., Israelow, B., et al. (2020). Longitudinal analyses reveal immunological misfiring in severe COVID-19. Nature 584, 463–469.
Mazaleuskaya, L., Veltrop, R., Ikpeze, N., Martin-Garcia, J., and Navas-Martin, S. (2012). Protective role of Toll-like Receptor 3-induced type I interferon in murine coronavirus infection of macrophages. Viruses 4, 901–923.
Mills, E.L., Kelly, B., Logan, A., Costa, A.S.H., Varma, M., Bryant, C.E., Tourlomousis, P., Däbritz, J.H.M., Gottlieb, E., Latorre, I., et al. (2016). Succinate dehydrogenase supports metabolic repurposing of mitochondria to drive inflammatory macrophages. Cell 167, 457–470.e13.
Mulchandani, R., Lyngdoh, T., and Kakkar, A.K. (2021). Deciphering the COVID-19 cytokine storm: systematic review and meta-analysis. Eur J Clin Invest 51, e13429.
Quinn, S.J., Ye, C.P., Diaz, R., Kifor, O., Bai, M., Vassilev, P., and Brown, E. (1997). The Ca^{2+}-sensing receptor: a target for polyamines. Am J Physiol Cell Physiol 273, C1315–C1323.
Rodriguez, A.E., Ducker, G.S., Billingham, L.K., Martinez, C.A., Mainolfi, N., Suri, V., Friedman, A., Manfredi, M.G., Weinberg, S.E., Rabinowitz, J.D., et al. (2019). Serine metabolism supports macrophage IL-1β production. Cell Metab 29, 1003–1011.e4.
Rogers, A.C., McDermott, F.D., Mohan, H.M., O'Connell, P.R., Winter, D.C., and Baird, A.W. (2015). The effects of polyamines on human colonic mucosal function. Eur J Pharmacol 764, 157–163.
Rosas, I.O., Bräu, N., Waters, M., Go, R.C., Hunter, B.D., Bhagani, S., Skiest, D., Aziz, M.S., Cooper, N., Douglas, I.S., et al. (2021). Tocilizumab in hospitalized patients with severe COVID-19 pneumonia. N Engl J Med 384, 1503–1516.
Sa Ribero, M., Jouvenet, N., Dreux, M., and Nisole, S. (2020). Interplay between SARS-CoV-2 and the type I interferon response. PLoS Pathog 16, e1008737.
Salama, C., Han, J., Yau, L., Reiss, W.G., Kramer, B., Neidhart, J.D., Criner, G.J., Kaplan-Lewis, E., Baden, R., Pandit, L., et al. (2021). Tocilizumab in patients hospitalized with COVID-19 pneumonia. N Engl J Med 384, 20–30.
Samuvel, D.J., Sundararaj, K.P., Nareika, A., Lopes-Virella, M.F., and Huang, Y. (2009). Lactate boosts TLR4 signaling and NF-κB pathway-mediated gene transcription in macrophages via monocarboxylate transporters and MD-2 up-regulation. J Immunol 182, 2476–2484.
Schultze, J.L., and Aschenbrenner, A.C. (2021). COVID-19 and the human innate immune system. Cell 184, 1671–1692.
Sette, A., and Crotty, S. (2021). Adaptive immunity to SARS-CoV-2 and COVID-19. Cell 184, 861–880.
Sha, W.C., Liou, H.C., Tuomanen, E.I., and Baltimore, D. (1995). Targeted disruption of the p50 subunit of NF-κB leads to multifocal defects in immune responses. Cell 80, 321–330.
Shen, B., Yi, X., Sun, Y., Bi, X., Du, J., Zhang, C., Quan, S., Zhang, F., Sun, R., Qian, L., et al. (2020). Proteomic and metabolomic characterization of COVID-19 patient sera. Cell 182, 59–72.e15.
Shui, G., Guan, X.L., Low, C.P., Chua, G.H., Goh, J.S.Y., Yang, H., and Wenk, M.R. (2010). Toward one step analysis of cellular lipidomes using liquid chromatography coupled with mass spectrometry: application to *Saccharomyces cerevisiae* and *Schizosaccharomyces* pombe lipidomics. Mol Biosyst 6, 1008–1017.
Siehler, S., Wang, Y., Fan, X., Windh, R.T., and Manning, D.R. (2001). Sphingosine 1-phosphate activates nuclear factor-κB through Edg receptors. J Biol Chem 276, 48733–48739.
Song, J.W., Lam, S.M., Fan, X., Cao, W.J., Wang, S.Y., Tian, H., Chua, G.H., Zhang, C., Meng, F.P., Xu, Z., et al. (2020). Omics-driven systems interrogation of metabolic dysregulation in COVID-19 pathogenesis. Cell Metab 32, 188–202.e5.
Thomas, T., Stefanoni, D., Reisz, J.A., Nemkov, T., Bertolone, L., Francis, R.O., Hudson, K.E., Zimring, J.C., Hansen, K.C., Hod, E.A., et al. (2020). COVID-19 infection alters kynurenine and fatty acid metabolism, correlating with IL-6 levels and renal status. JCI Insight 5.
Waggershauser, C.H., Tillack-Schreiber, C., Berchtold-Benchieb, C., Szokodi, D., Howaldt, S., and Ochsenkühn, T. (2020). Letter: immunotherapy in IBD patients in a SARS-CoV-2 endemic area. Aliment Pharmacol Ther 52, 898–899.
Wang, D., Hu, B., Hu, C., Zhu, F., Liu, X., Zhang, J., Wang, B., Xiang, H., Cheng, Z., Xiong, Y., et al. (2020a). Clinical characteristics of 138 hospitalized patients with 2019 novel coronavirus-infected pneumonia in Wuhan, China. JAMA 323, 1061–1069.
Wang, J., Jiang, M., Chen, X., and Montaner, L.J. (2020b). Cytokine storm and leukocyte changes in mild versus severe SARS-CoV-2 infection: review of 3939 COVID-19 patients in China and emerging pathogenesis and therapy concepts. J Leukoc Biol 108, 17–41.
Wu, P., Chen, D., Ding, W., Wu, P., Hou, H., Bai, Y., Zhou, Y., Li, K., Xiang, S., Liu, P., et al. (2021). The trans-omics landscape of COVID-19. Nat Commun 12, 4543.
Xia, H., Cao, Z., Xie, X., Zhang, X., Chen, J.Y.C., Wang, H., Menachery, V.

D., Rajsbaum, R., and Shi, P.Y. (2020). Evasion of type I interferon by SARS-CoV-2. Cell Rep 33, 108234.
Xiong, Y., Liu, Y., Cao, L., Wang, D., Guo, M., Jiang, A., Guo, D., Hu, W., Yang, J., Tang, Z., et al. (2020). Transcriptomic characteristics of bronchoalveolar lavage fluid and peripheral blood mononuclear cells in COVID-19 patients. Emerg Microbes Infect 9, 761–770.
Zhang, Q., Lenardo, M.J., and Baltimore, D. (2017). 30 Years of NF-κB: a blossoming of relevance to human pathobiology. Cell 168, 37–57.
Zheng, M., Karki, R., Williams, E.P., Yang, D., Fitzpatrick, E., Vogel, P., Jonsson, C.B., and Kanneganti, T.D. (2021). TLR2 senses the SARS-CoV-2 envelope protein to produce inflammatory cytokines. Nat Immunol 22, 829–838.

SUPPORTING INFORMATION

The supporting information is available online at https://doi.org/10.1007/s11427-021-2099-7. The supporting materials are published as submitted, without typesetting or editing. The responsibility for scientific accuracy and content remains entirely with the authors.